Journal of Power Sources 196 (2011) 4631–4637

Contents lists available at ScienceDirect

Journal of Power Sources

journal homepage: www.elsevier.com/locate/jpowsour

Large area high resolution neutron imaging detector for fuel cell research

Christian Tötzke[a,d,*], Ingo Manke[a], André Hilger[a], Gerard Choinka[a], Nikolay Kardjilov[a], Tobias Arlt[a], Henning Markötter[a], Alexander Schröder[b], Klaus Wippermann[b], Detlef Stolten[b], Christoph Hartnig[c,1], Phillip Krüger[c], Robert Kuhn[c], John Banhart[a,d]

[a] Helmholtz Centre Berlin (HZB), 14109 Berlin, Germany
[b] Research Centre Jülich (FZJ), 52428 Jülich, Germany
[c] Centre for Energy and Hydrogen Research (ZSW), 89081 Ulm, Germany
[d] Technical University Berlin, 10623 Berlin, Germany

ARTICLE INFO

Article history:
Received 11 November 2010
Received in revised form 7 January 2011
Accepted 16 January 2011
Available online 26 January 2011

Keywords:
Neutron imaging
Fuel cells
Water distribution
High resolution detector
Large field of view
Water management

ABSTRACT

Neutron radiography is increasingly being considered a powerful diagnostic tool in fuel cell research. Analyzing the water distribution for entire cells requires large and flexible fields of view and high spatial resolution at the same time. The combination of these requirements is a great technical challenge for neutron detectors: While conventional detectors could provide large fields of view, the accuracy of water mapping has so far been limited by their low spatial resolution. On the other hand, the applicability of sophisticated high-resolution detectors in fuel cell research is limited by their small and invariable fields of view.

We present a novel detector system designed to meet the specific demands of fuel cell research. High spatial resolution of at the best 25 μm was achieved by an optimized gadox scintillator, while a large and flexible field of view, e.g. 61.4 mm × 61.4 mm at a scale factor of 1:1 is provided by a 4096 × 4097 pixel^2 CCD-camera.

The set up ensures great adaptivity to fuel cells of various sizes along with the best possible spatial resolution. Studies on the water transport in a DMFC and PEMFC are presented to demonstrate the capacity of the detector system.

1. Introduction

Neutron radiography has been used as a valuable diagnostic technique in a wide range of industrial and scientific applications, providing complementary information to X-ray imaging [1–5]. The increasing number of publications related to neutron imaging is an indicator that it has become a standard tool for the investigation of fuel cell water distribution in polymer electrolyte membrane fuel cells (PEMFCs) [6–21] as well as CO_2- and cell water distribution in direct methanol fuel cells (DMFCs) [22,23].

Neutrons have unique properties for imaging when compared to X-rays: they can penetrate deeply into many metals, e.g. aluminum or steel, while they are strongly attenuated by hydrogen-containing compounds such as water. For the investigation of water distributions in engineering systems, neutron imaging is often favored over X-rays; although high-energy X-rays can penetrate metallic components, they only have low sensitivity to water and can therefore provide little information about the water distribution within a system.

So far the limited spatial resolution of neutron radiography has been one of the major drawbacks of this imaging technique. Three years ago, the typical resolution of standard imaging setups still ranged from 100 μm to 250 μm [1].

Alternatively, synchrotron X-ray radiography allows measurements at high spatial and temporal resolution [1]. This technique has been successfully applied to analyze water and carbon dioxide distributions in PEMFCs [24–28] and DMFCs [29]. In contrast to neutron radiography, only comparatively small cell areas of typically 10–100 mm^2 can be investigated due to the small field of view. In addition, all highly absorbent components must be removed from the beam path which necessitates modifications of the fuel cell design.

Several research groups have worked towards considerably improving the spatial resolution of neutron imaging. High-resolution neutron detector systems have been developed by

* Corresponding author at: Helmholtz Centre Berlin (HZB), Institute of Applied Materials, Hahn Meitner Platz 1, D-14109 Berlin, Germany. Tel.: +49 30 8062 42615; fax: +49 30 8062 42098.
E-mail address: christian.toetzke@helmholtz-berlin.de (C. Tötzke).
[1] Present address: Chemetall GmbH, Trakehner Straße 3, 60487 Frankfurt a.M., Germany.

0378-7753/$ – see front matter © 2011 Elsevier B.V. All rights reserved.
doi:10.1016/j.jpowsour.2011.01.049

following different engineering concepts. Prominent examples are micro-focusing optical devices [30] and imaging systems based on a ^{10}B-doped micro channel plate (MCP) [31,32] design. However, with respect to investigations of fuel cells, these high-resolution detector systems have a severe disadvantage: They provide only a small and invariable field of view (e.g. 27.6 mm × 27.6 mm, 14 mm × 14 mm or circular with 25 mm in diameter [30–32]). Thus, a vital advantage of conventional neutron detector systems over synchrotron X-rays, namely the wide field of view, is sacrificed in favor of higher spatial resolution. As studies on water management often require the visualization of large cell areas or even complete cells, time-consuming sequential screening procedures become necessary. Image scanning would have significant negative impacts on time resolution.

At the Helmholtz Centre in Berlin an alternative approach has been chosen: we have worked to develop a detector design based on conventional components that can cope with two major demands of fuel cell research: a large and flexible field of view and high spatial resolution at the same time. Such a system would allow for the visualization of large cell areas at high resolution without relying on intricate screening procedures.

2. Neutron detector imaging systems—state of the art

The basic components of a conventional modern neutron detector system are a low-noise CCD camera and a scintillator screen that converts detected neutrons into visible light. The sample under investigation is exposed to neutrons as close as possible to the scintillator. This way a 2D absorption image of the sample is formed on the scintillator screen and is subsequently projected onto the CCD-chip via a mirror and the lens system of the camera. The mirror prevents the camera from direct beam exposure. Images were recorded by a PC-system and later processed with appropriate software. The principal setup of a neutron radiographic study on fuel cells is depicted in Fig. 1.

Apart from beam parameters influencing the image resolution (i.e. collimation ratio L/D), the maximum spatial resolution of the detector system resolution is restricted by blurring on the scintillator screen, the optical quality of the camera lens and the pixel size on the CCD-chip.

Standard scintillator screens are coated with a powder mixture of lithium fluoride and zinc sulfide (^{6}LiFZnS). ^{6}Li-nuclei absorb impinging neutrons and as a result emit α and T (^{3}H) particles. In turn, these particles trigger photon-emitting scintillation events

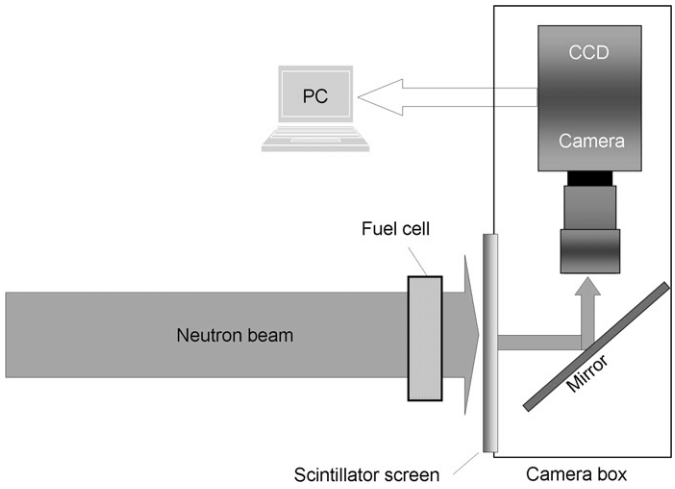

Fig. 1. Principal experimental setup for neutron radiographic studies of fuel cells.

as they interact with zinc sulfide particles; the scintillator starts shining.

The image definition of the sample projection formed by the scintillating screen depends on the thickness of the ^{6}LiFZnS layer and the mean free path of both T and α particles. Although thick coating layers ensure good light efficiencies (due to the high probability of neutron interaction with lithium nuclei), increasing the layer thickness impairs spatial resolution because of the extended travel of T and α particles and the increased effective size of photo-emission sites.

A reduction of 6LiFZnS layer thickness is, therefore, an obvious way to improve scintillator resolution. This also results in lower light efficiency requiring longer exposure times.

Taking into account the interrelationship of spatial and temporal resolution and the necessity to find a trade-off, the determination of the appropriate scintillator thickness depends on the requirements of the respective application.

3. Development of novel scintillator screens

The evolution of a high-resolution detector system is based on the improvement of the scintillator. The thickness of the ^{6}LiFZnS layer was reduced from 200 μm to 50 μm resulting in an

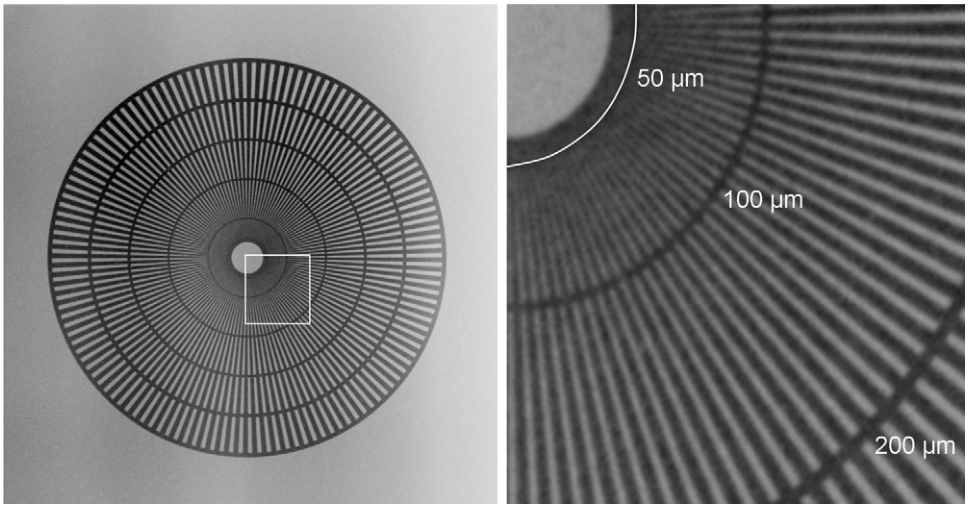

Fig. 2. Siemens star used in a resolution test. Left: image of the test pattern on a 10 μm gadox scintillator (200 mm lens, 150 s exposure time, 13.5 μm pixel size). Right: magnified detail of the area marked in white on the left, demonstrating a spatial resolution better than 50 μm.

improvement of the resolution from 137 μm to 72 μm. Images were taken by a CCD-camera (model Andor DW 436) in combination with a 105 mm Nikon lens. If the ^{6}LiFZnS layer thickness was further reduced, nearly all neutrons would pass through the scintillator screen without interaction, resulting in an unfavorable signal-to-noise ratio.

Yet a thinner scintillator design becomes possible if ^{6}LiFZnS is substituted by a Gd_2O_2S ("gadox") layer. Compared to ^{6}LiFZnS, gadox has a significantly larger effective cross section for neutrons. A layer of only 10-μm thick gadox absorbs nearly 90% of the incoming radiation.

A neutron captured by Gd generates conversion electrons that stimulate GdS_2O_3 to scintillate. The conditions for high spatial resolution are more favorable in gadox since the free mean path of conversion electrons (R_{ce} = 12 μm) is an order of magnitude less than that of T in ^{6}Li (R_t = 130 μm).

When used for neutron imaging, gadox scintillators also have some disadvantages, including high sensitivity to X-rays, and low light output due to the low energy of the conversion electrons. To compensate the latter drawback, the scintillator light output was optimized by embedding the gadox powder into water glass. Additionally, the incident neutron side of the scintillating layer was coated by an aluminum layer which back-reflects the light emitted away from the detector position. The performance of Gadox scintillators with layer thicknesses in the range of 5–30 μm was tested. Layer thickness between 10 and 20 μm was found to yield best light output. In thicker layers, self shielding occurs, which spoils the scintillator light performance.

As shown in Fig. 2, the scintillator resolution can be tested by imaging appropriate patterns, e.g. a Siemens star [33]. This test pattern consists of dark spokes on a bright background radiating from a common centre and getting wider towards the outside. The radial spokes of the star can be resolved from the outside of the pattern only down to a certain size, after which the central region is blurred. This provides an estimate for the spatial resolution.

Alternatively, the resolution can be determined using the modulation transfer function (MTF) which is calculated over a sharp edge. This was measured for an image produced by attaching a gadolinium foil to the scintillator. Resolution measurements achieved in this way for scintillators of various thicknesses are listed in Table 1. The results refer to a value of 10% of the MTF. Series consisting of three images, each with 30 s exposure time, were taken in order to compensate the low light emission and improve signal-to-noise ratios. "White spots" were reduced by median and erosion filters.

Table 1
Spatial resolutions of different gadox scintillators measured via the MTF of a sharp edge. Exposure time was 3 × 30 s in all cases.

Scintillator thickness [μm]	Resolution [μm]
30	61
20	40
10	31
5	25

4. Implementation of a 16 MegaPixel Camera System

Addressing questions of water management often requires the visualization of large cell areas or even complete cells, preferably at high resolution. The small and invariable field of view of most high resolution systems strongly restricts the practicability of such measurements: Since the dimensions of fuel cells normally exceed the image area a sequential scan is inevitable. This entails additional experimental effort and some loss of information about the water transport dynamics in the cell.

Upgrading the CCD-chip is a promising possibility to extend the image area. In combination with an appropriate lens system the field of view is now variable. At the Helmholtz Centre Berlin, this approach was realized by integrating a 4k × 4k CCD sensor based camera system (Peregrine 486) (Fig. 3).

A single pixel has a physical dimension of 15 μm × 15 μm. The camera is equipped with an optical system that allows a magnification range from 1:0.84 up to 1:1.25. At 1:1 scale, the field of view covers an area of 61.44 mm × 61.44 mm. Owing to the flexible magnification, the imaging field can be adapted to the requirements of a given application. A cooling system ensures the operation temperature of −50 °C, which is necessary to reduce thermal electronic noise.

When using gadox scintillators, longer exposure times must be accepted owing to the lower light output compared to ^{6}LiFZnS. However, the crucial neutron quantum yield is optimal, which improves the real signal statistics and largely compensates for this disadvantage.

Fig. 3. 16-MegaPixel-CCD Camera (Peregrine 486) equipped with a lens of the type Schneider Kreuznach Macro Symmar 5.6/120.

5. Applications in fuel cell research

Selected results of radiographic studies of the water distribution in a DMFC and PEMFC are presented in the following section. The experiments were conducted using the CONRAD instrument at the Hahn-Meitner research reactor of the Helmholtz Centre Berlin [34].

5.1. Water distribution in a running direct methanol fuel cell

5.1.1. Experimental setup

A direct methanol fuel cell was designed and manufactured at the Research Centre Jülich. The functional layers of the used membrane electrode assembly with an active area of 42 mm × 42 mm were prepared onto carbon cloth (Ballard). The anode and cathode electrode were hot-pressed on both sides of a Nafion N-115 membrane. One-molar methanol solution is fed to the anode side and distributed via a meandering channel structure. An air stream passes through the cathode where a matrix of square feet forms a grid flow field. In order to study the influence of surface treatments on the water transport characteristics, half of the cathode flow field surface was hydrophilized.

To allow for a radiographic study of the cell at high resolution and acceptable exposure times, a 20-μm thick gadox scintillator 45 mm × 45 mm in size was attached to the back of the cell. The 4k × 4k detector combined with a 1:0.84 optic is ideally suited for cells of this size. It provides a field of view of 51 mm × 51 mm at a pixel size of only 12.6 μm. This way, a high resolution is obtained without time consuming scanning of a detector with limited field of view.

5.1.2. Experimental results

Fig. 4 displays a series of quotient images of the test cell showing water distributions during 1 h of operation at a current density of 50 mA cm^{-2} and a cell temperature of 70 °C. The stoichiometric rates of the air and methanol stream with respect to the current density were $\lambda_{methanol} = 4$ and $\lambda_{air} = 4$, respectively. The dotted line indicates the border between untreated (left) and hydrophilized flowfield surface (right).

The water distribution was visualized by normalizing all images with respect to a reference state where the anode is flooded by methanol solution whereas the cathode side is dry.

Methanol solution is supplied to the bottom and exits at the top of the cell. The upward flow direction supports the drag out of CO_2 bubbles which form during operation. At the cathode side, air is fed in at the top of the cell.

The water formed at the cathode during cell operation is transported through the GDL and dragged out of the cell by both the gas stream and gravity. As illustrated in Fig. 4, the transport characteristics differ significantly between the untreated and hydrophilic cell area, respectively. While large water accumulation can be found inside the left (untreated) half of the cell, only much less water accumulates within the right half. This shows that the hydrophilic flow field offers good conditions for effective water transport. Water in the hydrophilic gas channels tends to form thin continuous layers covering the surface without severely interfering with the gas stream. In contrast, water forms droplets in the untreated part of the flowfield. The growing droplets successively flood the gas channels, thereby blocking gas flow. In Fig. 4, these flooded areas appear as dark rectangular spots revealing the checkered flow field geometry.

At the anode side, CO_2 bubbles are formed as product gas of methanol oxidation. The gas concentration in the anode channel increases in flow direction. Eventually, CO_2 exits the cell along with unreacted methanol solution. Even though the temporal resolution of the image series is insufficient to resolve single gas bubbles, the accumulation of CO_2 inside the gas channels can be tracked by analyzing the attenuation values along the anode channel. Fig. 5 shows a mean image of the test cell averaged over 1 h of operation which comprises 50 images with exposure times of 65 s, respectively.

Following the anode channel upwards, the transmission values successively increase, so the meandering anode channel appears brighter. This proves an increasing gas content in flow direction inside the channel.

In Fig. 6, the attenuation values are given along a line perpendicular to the meandering anode channel (as indicated in Fig. 5) with hatched areas indicating the channel regions. The trend of transmission along the channel clearly documents a bubble enrichment in the anode stream. The gradient suggests higher accumulation

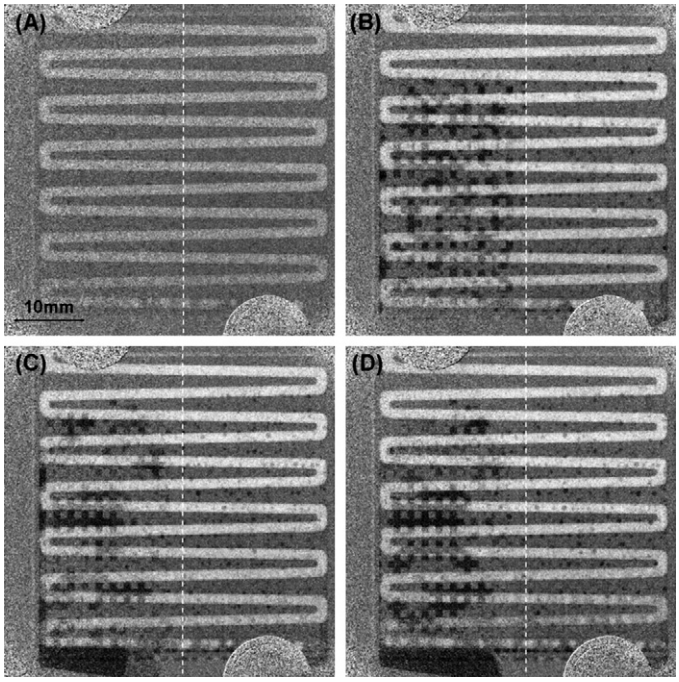

Fig. 4. Water formation and transport in a direct methanol fuel cell (DMFC) (current density 50 mA cm^{-2}, λ = 2): (A) start, (B) after 15 min, (C) after 30 min, and (D) after 60 min. Hydrophilic (right) and untreated areas are separated by the dashed line. Grey values < 1 (dark areas) indicate water accumulation.

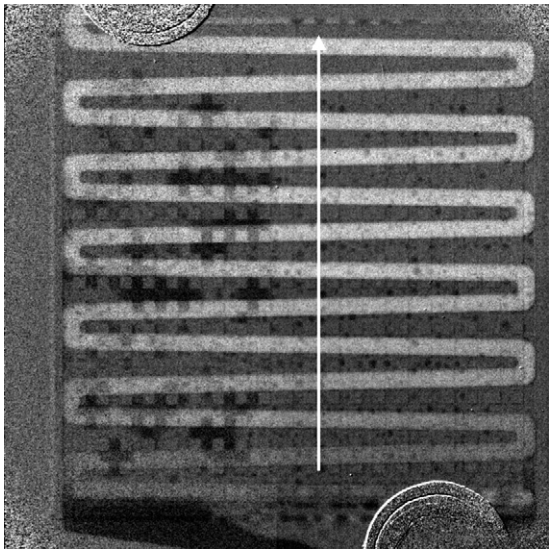

Fig. 5. Neutron image of the test cell averaged over 1 h of operation. Grey values along the white arrow are displayed in Fig. 6.

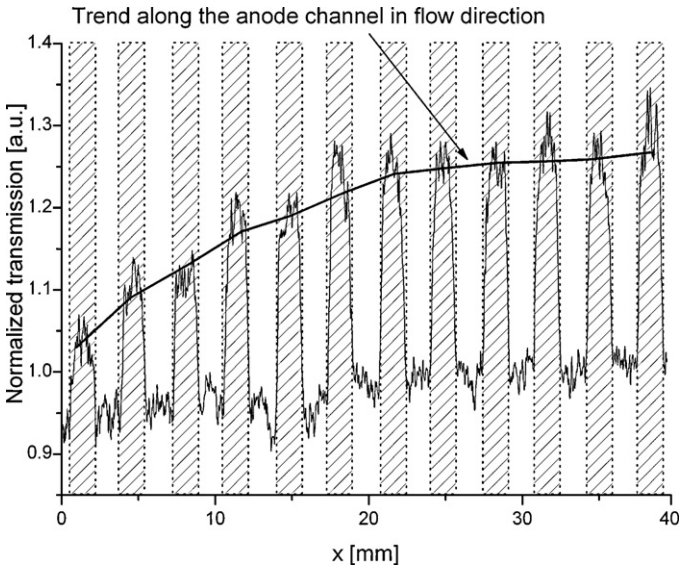

Fig. 6. Attenuation values along a line crossing the cell (white arrow in Fig. 5). Trend line represents downstream attenuation and reveals gas formation within the anode channel.

rates for the first half of the channel, which corresponds to the bottom half of the cell. Values in the unhatched regions of the diagram represent the transmission profile of the land areas along the arrow. The moderate increase in transmission indicates a decreasing water content of the GDL in from bottom to top.

5.2. Water distribution and eruptive water transport in a PEMFC

A study of the water distribution and transport in a polymer electrolyte membrane cell (PEM) is presented in a second example.

5.2.1. Experimental setup

The test cell was designed and manufactured at the Centre for Solar Energy and Hydrogen Research in Ulm (Germany). The cell dimension of 140 mm × 140 mm included an active area of 100 mm × 100 mm. A 420-μm thick gas diffusion layer (GDL) of the type "SGL 10 BB" was used. The media were distributed by a three-fold meander flowfield possessing 0.7-mm wide flow field channels separated by 0.8-mm wide land areas.

5.2.2. Experimental results

The test cell was operated through a series of increasing current densities: Starting in the dry condition at 100 mA cm^{-2}, the current density was successively increased to 300 mA cm^{-2} after 31 min, 400 mA cm^{-2} after 60 min and 500 mA cm^{-2} after 90 min after start. Throughout the experiment, the utilization rates were kept at u_C = 25% at the anodic and u_A = 90% at the cathodic side, the cell temperature was kept at 55 °C. Fig. 7 shows a series of representative quotient images documenting water evolution in both the GDL and the flow field channels. All images are normalized with respect to the reference image of the dry cell.

At the current density of 100 mA cm^{-2}, see Fig. 7(A), only a moderate amount of water is formed and accumulates inside the GDL, predominantly in the upper part of the cell beneath land areas. Very few droplets have entered the flowfield channels yet. Upon increasing the current density to 300 mA cm^{-2}, water accumulation in the GDL intensifies. Owing to the thickness of the GDL-type used, water diffusion inside the GDL can be tracked very well. The obvious grey shade in Fig. 7(B) indicates that water has now also accumulated in wide areas of the middle and lower test cell section. Moreover, first water droplets have entered flow field channels at various cites –

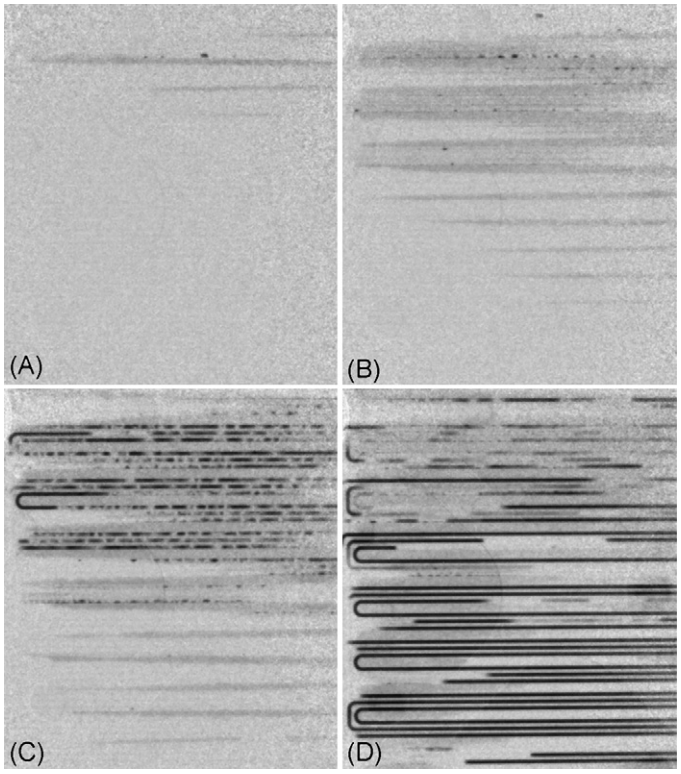

Fig. 7. Evolution of the water distribution at different current densities: (A) after 30 min, I = 100 mA cm^{-2}; (B) after 40 min, I = 300 mA cm^{-2}; (C) after 65 min, I = 400 mA cm^{-2}; (D) after 105 min, I = 500 mA cm^{-2}. Water accumulation within the GDL appears as grey shade, dark parts of the flowfield structure are the water filled channel sections.

recognizable as dark spots in Fig. 7(B). Further increasing the current density to 400 mA cm^{-2} and then to 500 mA cm^{-2} continues the trend of water accumulation, due to the formation rate now significantly exceeding the evaporation rate into the passing air stream. Consequently, channels are gradually flooded by coalescing water droplets that form growing water domains, which in turn

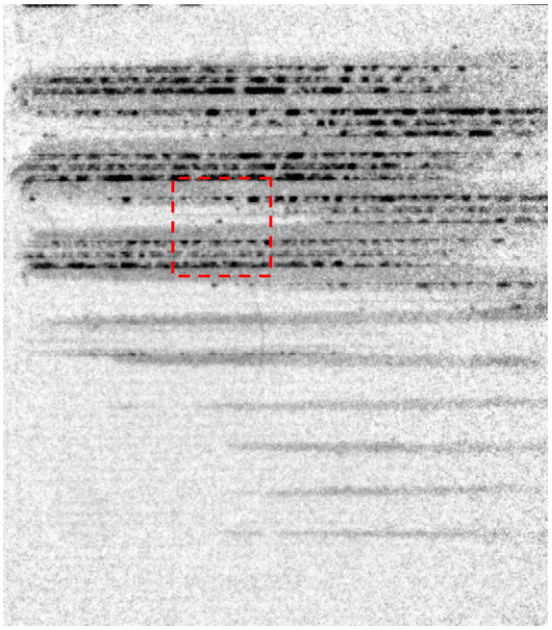

Fig. 8. Test cell operated at current density of 300 mA cm^{-2}, 58 min after start. At the centre of the designated area a transition spot is located.

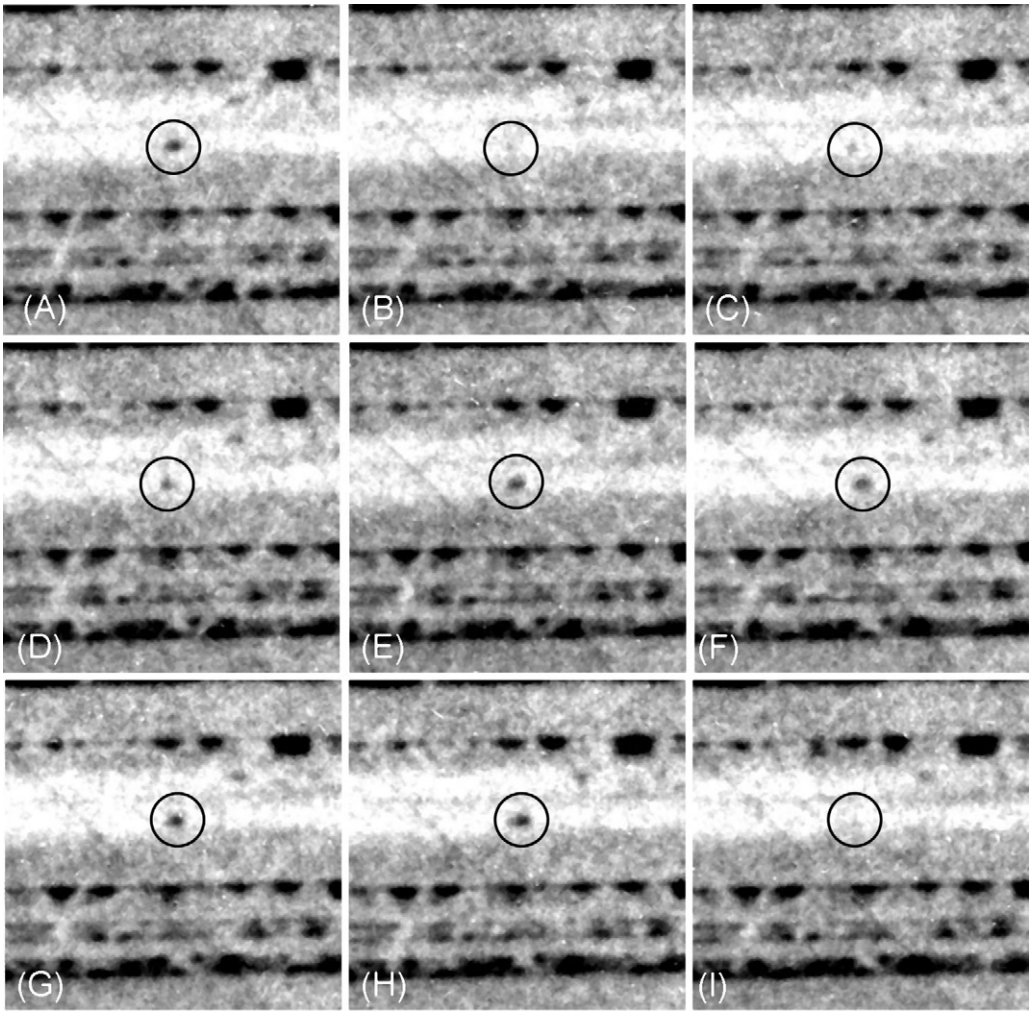

Fig. 9. Detail of the test cell showing eruptive water transport from the GDL into the flowfield channel.

extend to water columns. These water columns occupy complete channel sections and impede the bypass of air. Therefore, pressure builds up which eventually drags out entire cohesive water agglomerates, see Fig. 7(C) and (D).

An interesting water transport feature is the fast formation and stripping of droplets in the flow field channel [25,26,35–38]. Because the respective transition spots are very small and droplet transitions occur rapidly, the phenomenon of eruptive water transport from the GDL into the flowfield channels could be investigated *in situ* by synchrotron X-ray radiography only in the past [25,26].

In this neutron radiographic study it was possible to identify various spots at flowfield channels where water droplets form and disappear on a short time scale. The location of such a typical spot is highlighted by the dashed rectangular marker in Fig. 8.

A consecutive image series of the magnified detail highlighted in Fig. 8 is shown in Fig. 9. Images were exposed for 6 s and were triggered every 12 s. The location of droplet formation and stripping is highlighted by circular marks. Between Fig. 9(A) and (B) stripping of a droplet occurs. Subsequently, a new droplet forms and grows over a period of 66 s as shown in the image series Fig. 9(B) to (H) and, eventually, disappears again. The sudden disappearance suggests that droplets grow until they reach a critical size where they are either torn off by the air stream, Fig. 9(I), or a flush of water in the channel. The observation is in line with transport mechanism suggested by Litster et al. [38]. The spots of water expulsion mark final points of transport paths across the GDL. At these points,

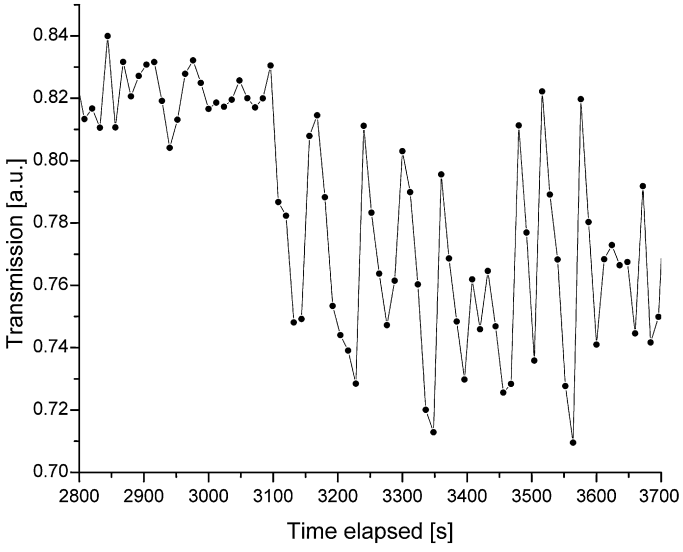

Fig. 10. Mean transmission values at the transition spot marked in Fig. 9. After 51 min, an intense oscillation sets in, indicating the sudden onset of droplet eruption.

the pressure build up inside the GDL induces the emergence and growth of water droplets.

An analysis of droplet growth and displacement shows that eruptive transport does not occur randomly, but rather shows regular temporal patterns. The intensity of the respective cell area (circular marks in Fig. 9) is shown in Fig. 10. After a run time of $t = 51$ min (3060 s), the intensity at the transition spot suddenly starts to oscillate. This oscillation is associated to the life time of droplets and has a periodicity of about 60 s ± 10 s. The experimental finding is also in line with experimental results of synchrotron X-ray radiographic studies that evidenced eruptive water transport into flowfield channels [25,26]. In previous studies, various spots of serial eruptive water expulsion with repetition times of typically 30–60 s were identified, which matches the order of magnitude found in the present neutron radiographic study [19].

6. Conclusions

Neutron radiography has been proven a valuable tool in fuel cell research. Neutrons have a high metal penetration potential and, concurrently, an excellent sensitivity to water. This makes them ideally suited for *in situ* studies of water management.

The development of novel gadox scintillators led to major improvements of the spatial resolution to 25 μm. In addition, the implementation of a 4k × 4k CCD chip allows for visualizing water distributions of large cell areas or even complete fuel cells with sizes ranging up to 73 mm × 73 mm at high spatial resolutions. When equipped with appropriate lens systems, the field of view could even be further extended to more than 200 mm × 200 mm.

A unique feature of the presented high-resolution detector system is the large and flexible field of view that can be adapted to fuel cells of various sizes while ensuring the best possible spatial resolution. As opposed to high-resolution detectors with a very limited field of view, intricate sequential screening procedures can be avoided.

Acknowledgements

The research activities were partly funded by the German Federal Ministry for Education and Science (BMBF) under grant number 03SF0324A and 03SF0324F (RuNPEM) and by the German Federation of Industrial Research Associations (AiF) under grant number 16002 N.

References

[1] J. Banhart, Advanced Tomographic Methods in Materials Research and Engineering, Oxford University Press, Oxford, UK, 2008.
[2] J. Banhart, A. Borbély, K. Dzieciol, F. Garcia-Moreno, I. Manke, N. Kardjilov, A.R. Kaysser-Pyzalla, M. Strobl, W. Treimer, International Journal of Materials Research (2010) 1069–1079.
[3] I. Manke, J. Banhart, A. Haibel, A. Rack, S. Zabler, N. Kardjilov, A. Hilger, A. Melzer, H. Riesemeier, Applied Physics Letters 90 (2007) 214102.
[4] N. Kardjilov, A. Hilger, I. Manke, M. Strobl, W. Treimer, J. Banhart, Nuclear Instruments and Methods in Physics Research Section A: Accelerators, Spectrometers, Detectors and Associated Equipment 542 (2005) 16–21.
[5] M. Strobl, I. Manke, N. Kardjilov, A. Hilger, M. Dawson, J. Banhart, Journal of Physics D-Applied Physics 42 (2009).
[6] R.J. Bellows, M.Y. Lin, M. Arif, A.K. Thompson, D. Jacobson, Journal of the Electrochemical Society 146 (1999) 1099–1103.
[7] R. Satija, D.L. Jacobson, M. Arif, S.A. Werner, Journal of Power Sources 129 (2004) 238–245.
[8] M.A. Hickner, N.P. Siegel, K.S. Chen, D.N. McBrayer, D.S. Hussey, D.L. Jacobson, M. Arif, Journal of the Electrochemical Society 153 (2006) A902–A908.
[9] J. Zhang, D. Kramer, R. Shimoi, Y. Ono, E. Lehmann, A. Wokaun, K. Shinohara, G.G. Scherer, Electrochimica Acta 51 (2006) 2715–2727.
[10] D. Kramer, J. Zhang, R. Shimoi, E. Lehmann, A. Wokaun, K. Shinohara, G.G. Scherer, Electrochimica Acta 50 (2005) 2603–2614.
[11] A. Turhan, K. Heller, J.S. Brenizer, M.M. Mench, Journal of Power Sources 160 (2006) 1195–1203.
[12] J.J. Kowal, A. Turhan, K. Heller, J. Brenizer, M.M. Mench, Journal of the Electrochemical Society 153 (2006) A1971–A1978.
[13] M.A. Hickner, N.P. Siegel, K.S. Chen, D.S. Hussey, D.L. Jacobson, M. Arif, Journal of the Electrochemical Society 155 (2008) B427–B434.
[14] P. Boillat, D. Kramer, B.C. Seyfang, G. Frei, E. Lehmann, G.G. Scherer, A. Wokaun, Y. Ichikawa, Y. Tasaki, K. Shinohara, Electrochemistry Communications 10 (2008) 546–550.
[15] C. Hartnig, I. Manke, N. Kardjilov, A. Hilger, M. Grünerbel, J. Kaczerowski, J. Banhart, W. Lehnert, Journal of Power Sources 176 (2008) 452–459.
[16] A. Geiger, A. Tsukada, E. Lehmann, P. Vontobel, A. Wokaun, G. Scherer, Fuel Cells 2 (2002) 92–98.
[17] I. Manke, C. Hartnig, N. Kardjilov, M. Messerschmidt, A. Hilger, M. Strobl, W. Lehnert, J. Banhart, Applied Physics Letters 92 (2008) 244101.
[18] D.J. Ludlow, C.M. Calebrese, S.H. Yu, C.S. Dannehy, D.L. Jacobson, D.S. Hussey, M. Arif, M.K. Jensen, G.A. Eisman, Journal of Power Sources 162 (2006) 271–278.
[19] I. Manke, C. Hartnig, M. Grunerbel, J. Kaczerowski, W. Lehnert, N. Kardjilov, A. Hilger, J. Banhart, W. Treimer, M. Strobl, Applied Physics Letters 90 (2007) 184101.
[20] J.P. Owejan, T.A. Trabold, D.L. Jacobson, D.R. Baker, D.S. Hussey, M. Arif, International Journal of Heat and Mass Transfer 49 (2006) 4721–4731.
[21] P. Boillat, G.G. Scherer, A. Wokaun, G. Frei, E.H. Lehmann, Electrochemistry Communications 10 (2008) 1311–1314.
[22] A. Schröder, K. Wippermann, J. Mergel, W. Lehnert, D. Stolten, T. Sanders, T. Baumhöfer, D.U. Sauer, I. Manke, N. Kardjilov, A. Hilger, J. Schloesser, J. Banhart, C. Hartnig, Electrochemistry Communications 11 (2009) 1606–1609.
[23] A. Schröder, K. Wippermann, W. Lehnert, D. Stolten, T. Sanders, T. Baumhöfer, N. Kardjilov, A. Hilger, J. Banhart, I. Manke, Journal of Power Sources 195 (2010) 4765–4771.
[24] C. Hartnig, I. Manke, R. Kuhn, S. Kleinau, J. Goebbels, J. Banhart, Journal of Power Sources 188 (2009) 468–474.
[25] I. Manke, C. Hartnig, N. Kardjilov, H. Riesemeier, J. Goebbels, R. Kuhn, P. Krüger, J. Banhart, Fuel Cells 10 (2010) 26–34.
[26] C. Hartnig, I. Manke, R. Kuhn, N. Kardjilov, J. Banhart, W. Lehnert, Applied Physics Letters 92 (2008) 134106.
[27] I. Manke, C. Hartnig, M. Grunerbel, W. Lehnert, N. Kardjilov, A. Haibel, A. Hilger, J. Banhart, H. Riesemeier, Applied Physics Letters 90 (2007) 174105.
[28] S.J. Lee, N.-Y. Lim, S. Kim, G.-G. Park, C.-S. Kim, Journal of Power Sources 185 (2008) 867–870.
[29] C. Hartnig, I. Manke, J. Schloesser, P. Krüger, R. Kuhn, H. Riesemeier, K. Wippermann, J. Banhart, Electrochemistry Communications 11 (2009) 1559–1562.
[30] E.H. Lehmann, G. Frei, G. Kühne, P. Boillat, Nuclear Instruments and Methods in Physics Research Section A: Accelerators, Spectrometers, Detectors and Associated Equipment 576 (2007) 389–396.
[31] A.S. Tremsin, J.V. Vallerga, J.B. McPhate, O.H.W. Siegmund, W.B. Feller, L. Crow, R.G. Cooper, Nuclear Instruments and Methods in Physics Research Section A: Accelerators, Spectrometers, Detectors and Associated Equipment 592 (2008) 374–384.
[32] O.H.W. Siegmund, J.V. Vallerga, A. Martin, B. Feller, M. Arif, D.S. Hussey, D.L. Jacobson, Nuclear Instruments and Methods in Physics Research Section A: Accelerators, Spectrometers, Detectors and Associated Equipment 579 (2007) 188–191.
[33] C. Grunzweig, G. Frei, E. Lehmann, G. Kuhne, C. David, Review of Scientific Instruments 78 (2007) 053708.
[34] N. Kardjilov, A. Hilger, I. Manke, M. Strobl, M. Dawson, J. Banhart, Nuclear Instruments and Methods in Physics Research Section A: Accelerators, Spectrometers, Detectors and Associated Equipment 605 (2009) 13–15.
[35] A. Bazylak, D. Sinton, N. Djilali, Journal of Power Sources 176 (2008) 240–246.
[36] P. Zhou, C.W. Wu, Journal of Power Sources 195 (2010) 1408–1415.
[37] P.K. Sinha, C.-Y. Wang, Electrochimica Acta 52 (2007) 7936–7945.
[38] S. Litster, D. Sinton, N. Djilali, Journal of Power Sources 154 (2006) 95–105.